



**HAL**  
open science

# Electroactive Area from Porous Oxide Films Loaded with Silver Nanoparticles: Electrochemical and Electron Tomography Observations

Nelly Couzon, Lucian Roiban, Fernand Chassagneux, Laurence Bois, Arnaud Brioude, Mathieu Maillard

► **To cite this version:**

Nelly Couzon, Lucian Roiban, Fernand Chassagneux, Laurence Bois, Arnaud Brioude, et al.. Electroactive Area from Porous Oxide Films Loaded with Silver Nanoparticles: Electrochemical and Electron Tomography Observations. ACS Applied Materials & Interfaces, 2019, 11 (40), pp.37270-37278. 10.1021/acsami.9b11581 . hal-02360162

**HAL Id: hal-02360162**

**<https://hal.science/hal-02360162>**

Submitted on 13 Jul 2022

**HAL** is a multi-disciplinary open access archive for the deposit and dissemination of scientific research documents, whether they are published or not. The documents may come from teaching and research institutions in France or abroad, or from public or private research centers.

L'archive ouverte pluridisciplinaire **HAL**, est destinée au dépôt et à la diffusion de documents scientifiques de niveau recherche, publiés ou non, émanant des établissements d'enseignement et de recherche français ou étrangers, des laboratoires publics ou privés.

# Electroactive Area from Porous Oxide Films loaded with Silver Nanoparticles: Electrochemical and Electron Tomography Observations

*Nelly Couzon<sup>a</sup>, Lucian Roiban<sup>b</sup>, Fernand Chassagneux<sup>a</sup>, Laurence Bois<sup>a</sup>, Arnaud Brioude<sup>a</sup>, Mathieu Maillard<sup>a</sup> \**

<sup>a</sup> Univ. Lyon, Université Claude Bernard Lyon 1, CNRS, Laboratoire des Multimatériaux et Interfaces, F-69622 Villeurbanne, France

<sup>b</sup> Univ. Lyon, INSA-Lyon, Université Claude Bernard Lyon I, MATEIS, UMR5510 CNRS, 7 avenue Jean Capelle, 69100 Villeurbanne, France

KEYWORDS: Silver nanoparticles, mesoporous film, cyclic voltammetry, electroactive area, STEM electron tomography

## ABSTRACT

Electrochemical studies of nano-material-based electrodes have been widely developed for catalyst and energy harvesting applications. The evolution of these electrodes over time and their efficiency have been very much studied and analyzed in order to optimize their performance. However, the electrochemical responses of electrodes are rarely studied in terms of the position of the active species within these electrodes. In this paper, we highlight that the spatial location of silver NPs

embedded inside semi-conductive porous films,  $\text{TiO}_2$  or  $\text{Fe}_2\text{O}_3$ , is crucial for the electrochemical response. In fact, by using cycling voltammetry and electron tomography experiments, we show the existence of an “electroactive area”, corresponding to a reduced thickness of the sample in close vicinity to a FTO (Fluorine doped Tin Oxide) substrate where most of the electrochemical responses originate. Our results demonstrate that, for a film thickness of several hundred nanometers, only less than 30 nm close to the substrate responds electrochemically. However, cyclic voltammetry empties the electroactive area of silver NPs. Therefore, application of chrono-amperometry coupled to an irradiation allowed regeneration of this area, thanks to an increased diffusion of silver species. In this paper, we also show the significant diffusion of silver species within the film during electrochemical experiments, phenomenon even increased by irradiation. These results are therefore an important step that shows the importance of the localization of active species within porous film and help in understanding and increasing the durability of nano-material-based electrodes.

## INTRODUCTION

Nanomaterials are very interesting due to their outstanding properties for heterogeneous catalysis<sup>1</sup> and energy harvesting,<sup>2,3</sup> allowing higher efficiency and lower manufacturing costs due to their small size. In particular, metallic NPs exhibit unusual optical property enhancement due to plasmon resonance,<sup>4</sup> related to size, shape and distribution of NPs within solid matrices.<sup>5-7</sup> Anchoring these NPs on the latter is thus a critical step in optimizing both accessibility to NPs and durability of the composite material. One of the usual methods to create strong interactions between NPs, their matrices and the surrounding environment consists in embedding the NPs in a mesoporous material. These materials have interesting properties such as controlled porosity and high specific surface area which make them a good support for retaining NPs.<sup>8</sup> At the same time, they allow a large interaction between these NPs and the surrounding media, such as a reactive gas or electrolyte.<sup>9</sup> One spectacular example of the possible interaction between a semi-conductive matrix, the NPs and

the surrounding environment is the photochromic behavior of Ag NPs dispersed in mesoporous TiO<sub>2</sub>.<sup>10-12</sup> In this case, visible light induces a photo-oxidation reaction of silver due to a plasmon induced electron transfer between the metallic NP and the semi-conductive host, and acts as a reversible, photosensitive support for information storage. In the domain of catalysis and electro-catalysts, the evolution of NPs is still a major industrial issue as it has been proven that properties are usually strongly affected by the fact that particles evolve during the catalytic process, inducing migration and size and shape evolution,<sup>13,14</sup> also known as catalysis leaching.<sup>15,16</sup> This usually leads to a significant reduction in material properties and is therefore a major drawback for most industrial applications. Catalysts are extremely small particles embedded in a solid matrix and are therefore difficult to observe in situ. In addition, it can be hard to evaluate their migration on a large scale in order to understand and remedy end-user reliability issues.

In this paper, we focused on two mesoporous semi-conductive oxides: TiO<sub>2</sub> and  $\alpha$ -Fe<sub>2</sub>O<sub>3</sub>. One of the easiest methods to prepare mesoporous thin films is the evaporation induced self-assembly (EISA) process, first reported by Brinker's group.<sup>17,18</sup> TiO<sub>2</sub> possesses a wide band gap of 3-3.2 eV and is currently one of the most studied semiconductors, due to its strong photo-catalytic activity, first discovered by Fujishima and Honda in 1972.<sup>19</sup> Fe<sub>2</sub>O<sub>3</sub> possesses a lower band gap (2,2 eV) which allows a strong absorption on a large portion of the solar spectrum and is an interesting candidate for photo-catalysis, as well.<sup>20</sup>

A common problem with Ag species is their reactivity and their tendency to dissolve and diffuse in and out of mesoporous films. An example of this behavior is the Ostwald ripening of silver NPs<sup>21</sup>, with the growth of the largest particles at the expense of the smaller ones. Under electrochemical conditions, this effect is clearly observable and enhanced, as a shift of silver redox potential depends on the size of NPs.<sup>22</sup> Light irradiation of silver NPs with an external electric field can also induce structural change.<sup>23</sup> Ag species have also showed reactivity toward O<sub>2</sub>, with a diffusion of oxygen atoms in the subsurface of silver.<sup>24</sup>

The evolution of Ag NPs is generally studied in terms of time and environment. However, the importance of the NP position compared to the substrate with respect to the electrochemical response is rarely considered. Therefore, in this report, the electrochemical activity of silver NPs has been investigated depending on their position in the mesoporous film and whether irradiation is applied or not. Based on the cyclic voltammetry (CV) results, this study highlights the existence of an electroactive zone in the area close to FTO, corresponding to a small area from where the electrochemical response is obtained. Furthermore, we have used electron tomography (ET) to quantify the Ag NPs and determine their position within the TiO<sub>2</sub> mesoporous matrix, before and after photo-electrochemical experiments in order to evaluate and understand the mobility of silver species during CV experiments.

## EXPERIMENTAL SECTION

### Materials

Two poly(ethylene oxide)-poly(propylene oxide)-poly(ethylene oxide) block copolymers, Pluronic F 127 ((EO)<sub>106</sub>-(PO)<sub>70</sub>-(EO)<sub>106</sub>) and Pluronic P 123 ((EO)<sub>20</sub>-(PO)<sub>70</sub>-(EO)<sub>20</sub>), iron (III) nitrate nonahydrate (Fe(NO<sub>3</sub>)<sub>3</sub>·9H<sub>2</sub>O), titanium butoxide Ti(OBu)<sub>4</sub>, hydrochloric acid HCl, silver nitrate (AgNO<sub>3</sub>) and formaldehyde (CH<sub>2</sub>O) were all purchased from Sigma-Aldrich and used as received. The FTO (fluorine-doped tin oxide) substrate (3 × 3 cm, 600 nm of FTO-deposited by CVD deposited on glass) was purchased from Solems.

### Electrode preparation:

For Fe<sub>2</sub>O<sub>3</sub> electrodes, the coating solutions were prepared by mixing Fe(NO<sub>3</sub>)<sub>3</sub>·9H<sub>2</sub>O, ethanol, water and triblock copolymer, F127. The molar ratio for Fe(NO<sub>3</sub>)<sub>3</sub>·9H<sub>2</sub>O/F127/H<sub>2</sub>O/EtOH is 1/0.01/7/29. After stirring the solution for half an hour, films were then deposited by a dip-coating

method on the FTO substrates, with a withdrawal speed of 2 mm.s<sup>-1</sup>. The films were aged under ambient conditions (T = 23 °C, RH = 30-40%) for 24 h and then calcined at 500°C for 4 h, with a heating ramp of 1 °C. min<sup>-1</sup>. For the TiO<sub>2</sub> mesoporous film, synthesis was performed according to previously published results.<sup>25</sup>

In order to form silver NPs inside the porous hematite or mesoporous titania film, the films were immersed in an ammoniacal silver nitrate solution ([Ag(NH<sub>3</sub>)<sub>2</sub>]<sup>+</sup>NO<sub>3</sub><sup>-</sup>, 50 mM) for 15 min. Then, the films were immersed for 15 min at 80 °C in a solution of 12 mM of formaldehyde in ethanol in order to chemically reduce silver ions into silver NPs. The resulting films were stored in a dark place in ambient conditions prior to photo-electrochemical measurements.

For porosity measurements, TiO<sub>2</sub> and Fe<sub>2</sub>O<sub>3</sub> powder were obtained using the same preparation method described above except that oxides were prepared directly in the glass vials, without dip-coating. The solutions obtained were heated at 50°C for 2 days then the obtained solid was calcined at 400 °C during 4 h for TiO<sub>2</sub> and 500 °C during 4 h for Fe<sub>2</sub>O<sub>3</sub>, with a heating ramp of 1 °C.min<sup>-1</sup>.

### **Characterization:**

Scanning electron microscopy (SEM) images were obtained using a Zeiss Merlin Compact SEM with an in-lens detector at a low acceleration voltage of 5 kV. Energy dispersive X-ray analysis (EDS) was used to determine the amount of silver within the films. The UV-visible absorption spectra of prepared samples were obtained using a Safas UVmc spectrometer measuring absorbance from films under direct incidence. Scans were measured between 300 and 1000 nm, with a 2 nm resolution. Grazing angle X-Ray Diffraction patterns were acquired with a D8 Discover with monochromatic copper radiation ( $\lambda = 1.542 \text{ \AA}$ ), from 10° to 70° to study the crystalline structure of our films. Textural characterizations were realized using nitrogen adsorption/desorption isotherms on a BelsorpMini (Bel Instruments, Japan). Prior to analysis, samples were outgassed under vacuum (at 100 °C for 4 h). Pore size distribution (max radius) and mesoporous volume were calculated from the adsorption branch of the isotherms using the Barrett-Joyner-Halenda (BJH) method. The

total porous volume was measured at  $P/P_0=0.98$ . The surface area was determined by the Brunauer-Emmett-Teller (BET) approach. Ellipsometric parameter measurements were performed with an atmospheric multiwavelength Ellipso-Porosimeter EP-A SOPRA GES 5E. The effective indexes and thicknesses of layers constituting films were calculated using a modified Cauchy-type dispersive law. For porosity measurements, water vapor was condensed in the film, at a relative humidity (RH) varying from 0 to 98%. From the effective index at the chosen wavelength of 633 nm, the volume fraction of condensed water is calculated using the Lorentz–Lorenz law and is represented as a function of RH. The pore size distribution (PSD) is then obtained using the Kelvin relation. The thickness of the films was measured using a Dektat profiler.

All electrochemical measurements were performed using an Orignalys OGS080 Potentiostat with a three-electrode cell designed by Zahner GmbH. A spiral Pt wire was used as the counter electrode and the reference electrode was a Re-5B Ag/AgCl electrode from BASi with a potential of 0.21 V/NHE. The working electrode was our titania or hematite-Ag film deposited on the FTO substrate ( $3 \times 3$  cm). The contact area between the film and the electrolyte is a circle of about  $3.6 \text{ cm}^2$ . LED's at 360 nm and white light were purchased from LED ENGINE Co. and calibrated with a flame spectrometer from Ocean Optic<sup>25</sup>. Their nominal flux was 340 and 1300 lumens, respectively. Measurements were carried out in a neutral electrolyte,  $\text{Na}_2\text{SO}_4$  1 M, at room temperature. During illumination experiments, samples were irradiated from the back. A typical CV experiment was performed with a potential sweep rate of 100 mV/s between - 0.5 V and + 0.5 V.

Electron tomography was performed on an ETEM TITAN 80 -300 keV electron microscope in High Angle Annular Dark Field – Scanning Transmission Electron Microscopy mode (HAADF-STEM). The sample was scraped off of its support using a scalpel, dispersed in ethanol and then a droplet of the solution was laid on a holey carbon 200 mesh grid. The grid was then installed on a Fischione 2020 tomography holder and the sample was tilted from  $-74^\circ$  to  $74^\circ$  with an incremental step of  $2^\circ$ . Three samples were analyzed and for each a tilt series of 74 images of a resolution of  $2048 \times 2048$  pixels were recorded using the tomography plugin of the TIA software, a pixel

representing 0.5 nm. After recording, the tilt series were aligned using the Imod software<sup>26</sup>, the volumes were calculated using 15 iterations of algebraic reconstruction technique (ART)<sup>27</sup> implemented in the Tomoj<sup>28</sup> plugin of the ImageJ software.<sup>29</sup> The 3D visualization and quantification was done using tools implemented in ImageJ<sup>30-34</sup> and 3D Slicer.

## RESULTS

### **Characterization of films before photo-electrochemical measurements**

SEM images of TiO<sub>2</sub>-Ag film showed a mesoporous film with a wormlike structure (Figure 1a). Silver NPs were homogeneously distributed, with an average size of 15 nm on the surface of TiO<sub>2</sub> and a large size distribution (from 7 to 40 nm). Inside pores, silver NPs are smaller, with an average size of  $11.4 \pm 3$  nm, as show in Figure S1 a. Energy Dispersive X-ray Spectroscopy (EDS) analyses gave an atomic ratio of Ag/Ti at 0.30, showing that impregnation with silver salt was highly efficient. The thickness of the film, measured by ellipsometry and profilometry, was 200 nm. The porous volume was estimated at 45% using ellipsoporosimetry. Combining those data, the percentage of Ag present at the surface of the electrode was calculated as 1.7 % of the total amount of Ag, which means that particles at the surface represents a very small fraction of available silver and most of the particles are located within pores. More precisely, we determined that 18.5% of the pore volume of TiO<sub>2</sub> is filled with Ag NPs. Details of these calculations are presented in ESI 1, ESI 2 and Table S1.

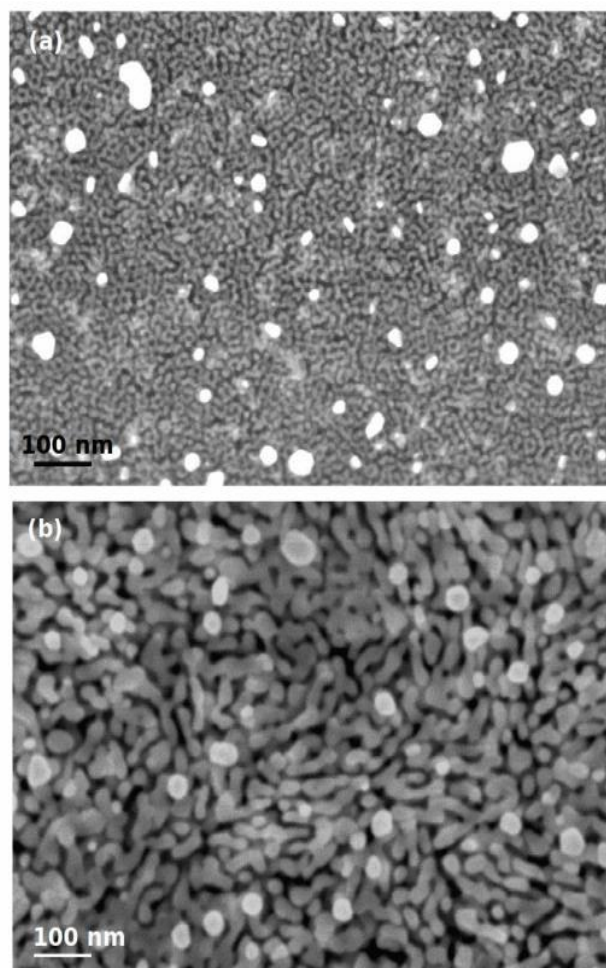


**Figure 1.** SEM pictures of mesoporous TiO<sub>2</sub>-Ag (a) and porous Fe<sub>2</sub>O<sub>3</sub>-Ag film (b)

As observed by SEM, the Fe<sub>2</sub>O<sub>3</sub>-Ag film exhibits larger pores than the TiO<sub>2</sub>-Ag one, and is therefore between a mesoporous and macroporous film. Silver NP sizes on the surface of the film range from 5 to 35 nm according to SEM pictures, with an average of  $17.5 \pm 5$  nm (Figure 1b). Inside the porous Fe<sub>2</sub>O<sub>3</sub> film, Ag NPs are smaller (Figure S1 b), with an average size of  $12 \pm 5$  nm. EDS analysis shows an atomic ratio for Ag/Fe of 0.13. Knowing that the thickness of the film is about 350 nm and porous volume is 46%, the percentage of silver present at the surface of the electrode is calculated as 2.6% of the total amount of silver, which is comparable to that obtained for the TiO<sub>2</sub>-Ag film. In both cases, this result implies that the majority of the silver NPs are embedded inside the porosity, and particles at the surface represent a very small fraction of the total silver amount ( $< 3$  % in both materials). In the case of Fe<sub>2</sub>O<sub>3</sub> film, we determine that only 10 % of the pores are filled with Ag NPs. A summary of these analyses is presented in Table 1.

**Table 1.** Summary of the TiO<sub>2</sub>-Ag and Fe<sub>2</sub>O<sub>3</sub>-Ag film characteristics

	Ag-TiO <sub>2</sub>	Ag-Fe <sub>2</sub> O <sub>3</sub>
Thickness (nm)	200 ± 15	350 ± 20
Porosity (%)	45 ± 5	46 ± 5
Average pore size (nm)	10 ± 2	42 ± 8
Atomic ratio Ag/Ti	0.30 ± 0.02	0.13 ± 0.02
Ag NP size (nm) (surface)	15 ± 5	17.5 ± 5
Ag NP size (nm) (inside pores)	11.4 ± 3	12 ± 4
% pores filled by Ag NPs	18.5	10
% of silver located at the surface	1.7	2.6

Film porosity was characterized by measuring the adsorption/desorption isotherm of the equivalent powder (Figure 2). For TiO<sub>2</sub>, a mesoporous volume of 0.25 cm<sup>3</sup>/g and a specific area of 97 m<sup>2</sup>/g were measured. On average, the pore size is 10 nm. The texture of the iron oxide is identified as close to macroporous by SEM, which is confirmed here: the BJH analysis gave an average pore size of 42 nm. The specific surface area is low 28 m<sup>2</sup>/g and the porous volume is 0.18 cm<sup>3</sup>/g.

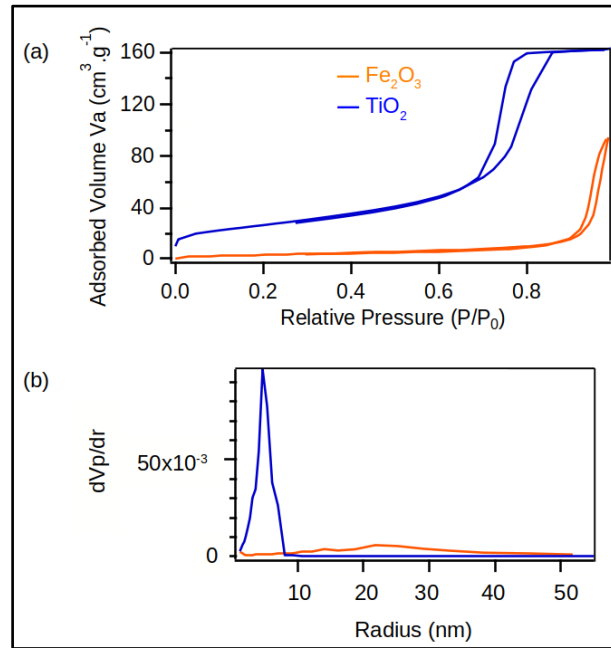
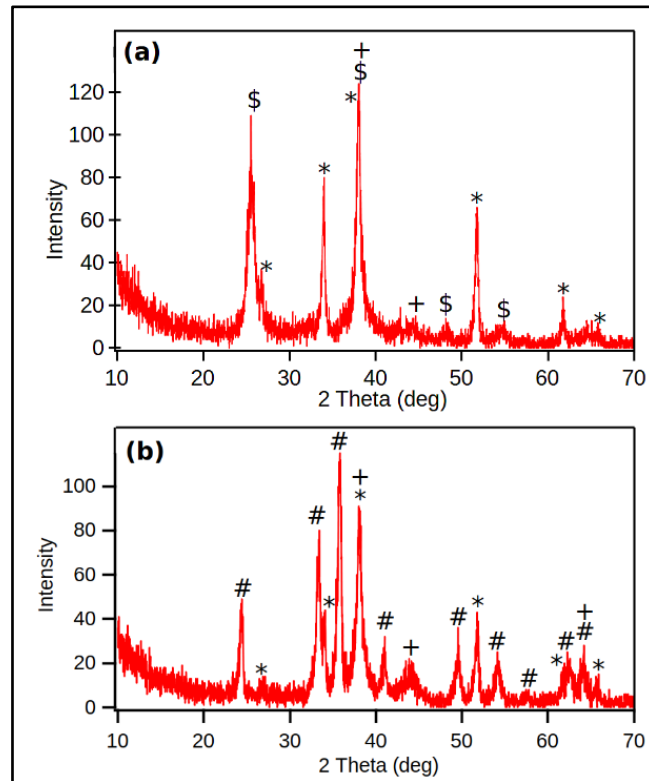


**Figure 2.** Adsorption/Desorption isotherms (a) and BJH adsorption distribution (b) of  $\text{Fe}_2\text{O}_3$  (orange) and  $\text{TiO}_2$  (blue) powder

To determine the crystallinity of the film, grazing angle XRD was used on the TiO<sub>2</sub>-Ag and Fe<sub>2</sub>O<sub>3</sub>-Ag films deposited on the FTO substrates (Figure 3). This technique was used to enhance the

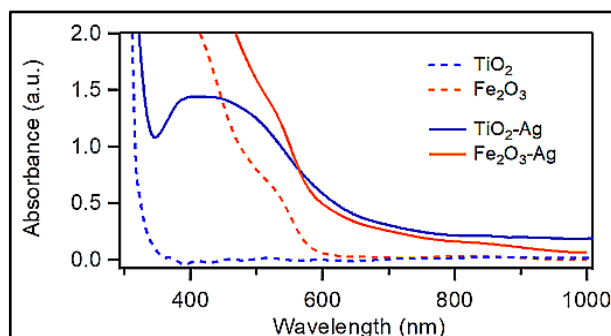


signal from the film compared to the highly crystallized FTO substrate.

**Figure 3.** Grazing angle XRD of (a) TiO<sub>2</sub>-Ag film and (b) Fe<sub>2</sub>O<sub>3</sub>-Ag film, where \$=Anatase TiO<sub>2</sub>, # =  $\alpha$ -Fe<sub>2</sub>O<sub>3</sub> Hematite, \* = Cassiterite SnO<sub>2</sub>, and + = Cubic Ag

As can be seen from Figure 3, the XRD results show several crystallized structures. First, cassiterite SnO<sub>2</sub> is still present as shown by the main peaks at 26.6° (110), 33.8° (100), 37.8° (200) and 51.8° (211) (File 01-077-0451). Second, TiO<sub>2</sub> is crystallized in the anatase phase, identified by peaks at 25.3° (101), 37.8° (004) and 48.2° (200) (File 01-089-4921) (Figure 3a). Third, the hematite phase is clearly present in the Fe<sub>2</sub>O<sub>3</sub> film with characteristic peaks at 23.8° (012), 33.2° (104) and 35.7° (110) (File 01-088-2359) (Figure 3b). Finally, cubic silver is weakly observed in both samples, with peaks at 38.2° (111) and 44.4° (200) (File 01-087-0720).

For both materials, the presence of silver NPs clearly increases the absorption of the film in the



visible region (Figure 4).

**Figure 4.** UV-Vis spectroscopy of TiO<sub>2</sub>-Ag (blue) and Fe<sub>2</sub>O<sub>3</sub>-Ag (orange) porous film.

In the TiO<sub>2</sub>, the formation of Ag NPs leads to a transition from a transparent to a brown-colored film. On the UV-visible spectrum, this is characterized by a large absorption peak at around 420-450 nm which is related to the SPR of Ag NPs. This peak is red-shifted compared to the usual peak of silver NPs observed in materials<sup>35</sup> and is attributed to two main factors: the high refractive index of titania (2.5)<sup>36</sup> and the existence of an interfacial charge transfer.<sup>37-40</sup>

In hematite, without silver NPs, the film is initially orange with a strong absorption (optical density >1 for  $\lambda < 480$  nm) and the addition of Ag NPs further increases the absorption and the film turns dark brown. Unfortunately, the absorption peak due to the surface plasmon resonance of silver NPs is screened by the strong initial absorption of the pristine hematite film.

### Photo-electrochemical Study

The first electrochemical experiments of TiO<sub>2</sub>-Ag and Fe<sub>2</sub>O<sub>3</sub>-Ag films were made with CV, with 100 cycles from - 0.5 V to + 0.5 V without light exposure and the results are given in Figure 5.

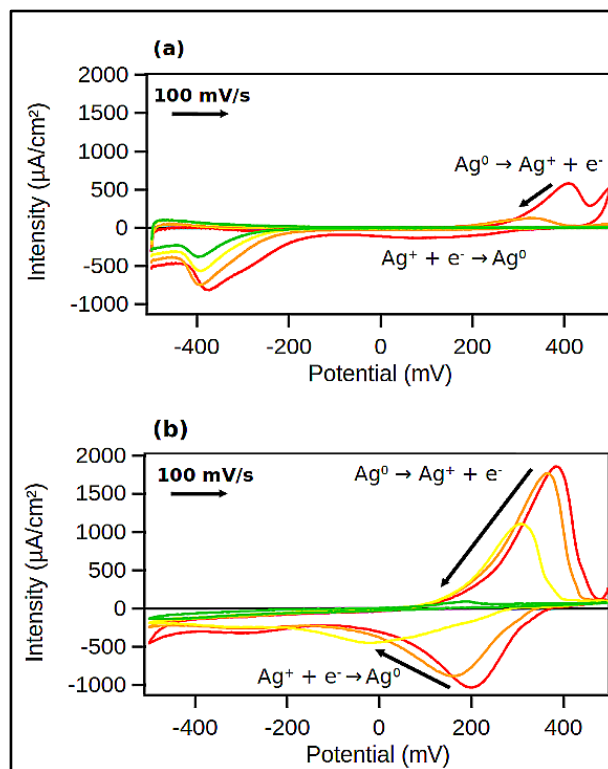


**Figure 5.** CV of (a) Fe<sub>2</sub>O<sub>3</sub>-Ag and (b) TiO<sub>2</sub>-Ag film; red curve: 1st cycle; orange: 3rd cycle; yellow: 10th cycle; green: 100th cycle (Electrolyte: Na<sub>2</sub>SO<sub>4</sub> 1M)

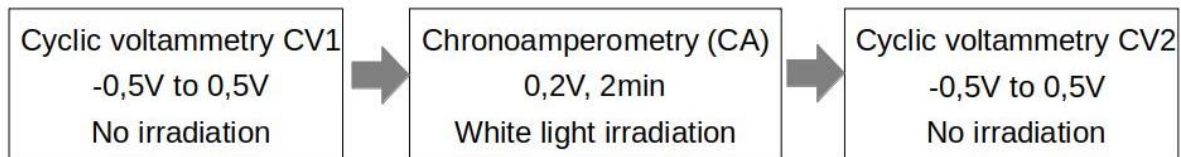
Both films show redox peaks of silver. In Fe<sub>2</sub>O<sub>3</sub>, we observe an oxidation peak at 400 mV on the first cycle, which correspond to  $\text{Ag}^0 \rightarrow \text{Ag}^+ + \text{e}^-$  (Figure 5a). We also observe the initiation of a second oxidation peak at 500 mV. These peaks rapidly decrease in intensity and potential, with a shift to 320 mV after 5 cycles. Reduction of silver ions appears only in the first cycle as a large wave between 100 and 200 mV. No further reduction peak can be observed in the next cycles. Globally, the redox peaks of silver in the Fe<sub>2</sub>O<sub>3</sub> porous film quickly disappear, in less than 10 cycles, indicating that the retention effect expected from porous materials seems limited in Fe<sub>2</sub>O<sub>3</sub>, as reactive species either leach out of the film or cannot react at the electrode interface. In addition, another reduction peak is observed at -370 mV and seems quite stable over all the cycles. This peak is only visible if silver NPs are present within the film (Figure S2). Without them, an intense cathodic wave is observed between -250 mV and -500mV. The stability and intensity of the reduction peak and also the absence of a corresponding oxidation peak led us to identify this as the irreversible reduction of Fe(III) to Fe(II) in iron oxide<sup>41</sup> catalyzed by silver NPs.

In the mesoporous film of TiO<sub>2</sub> containing silver NPs, their oxidation is observed at 390 mV and the reduction potential is around 200 mV during the first cycle. These silver redox potentials are close to what were observed in Fe<sub>2</sub>O<sub>3</sub>. The redox peak currents are more intense and can be explained by the higher concentration of Ag impregnated in TiO<sub>2</sub> compared to Fe<sub>2</sub>O<sub>3</sub> and a higher conductivity from TiO<sub>2</sub>. The evolution during cycling also shows a slower decrease in potential and intensity of silver redox peaks. After 100 cycles, a small oxidation peak of Ag NPs remains visible in TiO<sub>2</sub>. This could be attributed to a higher retention efficiency of silver species from TiO<sub>2</sub>, linked to a smaller porosity of titania and/or a higher affinity between Ag<sup>+</sup> and TiO<sub>2</sub> than between Ag<sup>+</sup> and Fe<sub>2</sub>O<sub>3</sub>.

In both cases, the redox peak intensity from silver decreases until it total disappears. We could therefore assume that Ag species progressively diffuse out of the film and into the electrolyte solution. However, SEM and EDS analyses show that the silver content decreases slightly and Ag NPs are observed at the surface of the film (Figure S3). Silver NPs on Fe<sub>2</sub>O<sub>3</sub> film are still around 15 ± 5 nm with a molar ratio of Ag/Fe of 0.09 whereas in TiO<sub>2</sub> film, Ag NP are about 17 ± 10 nm and the molar ratio is 0.28.

To increase our understanding of what is happening during CV, we calculated the fraction of silver available for the redox electrochemical reactions based on the CV results in Figure 5, as we know the total amount of silver within each film and the amount of silver oxidized during CV. The details of these calculations are presented in ESI 3 and Table S2. For the TiO<sub>2</sub> sample, only 15% of the total silver is oxidized in the first CV cycle (red curve Figure 5b). In the Fe<sub>2</sub>O<sub>3</sub> sample, we find that 6.5 % of the silver is oxidized in the first cycle (red curve Figure 5a). If we consider a sample where silver is initially homogeneously distributed within the sample, we can therefore estimate that approximately 28 nm of the film thickness of TiO<sub>2</sub>-Ag is impacted and 23 nm for Fe<sub>2</sub>O<sub>3</sub>-Ag film (for a film thickness of 200nm and 350 nm, respectively).

The rapid disappearance of silver redox peaks in electrochemical experiments, especially for  $\text{Fe}_2\text{O}_3\text{-Ag}$ , can be an issue for the characterization of the electrode. However, the addition of a chrono-amperometry (CA) sequence under irradiation between two CV sequences shows surprising



results (Scheme 1, Figure 6 and Figure S4).

**Scheme 1.** Electrochemical sequences

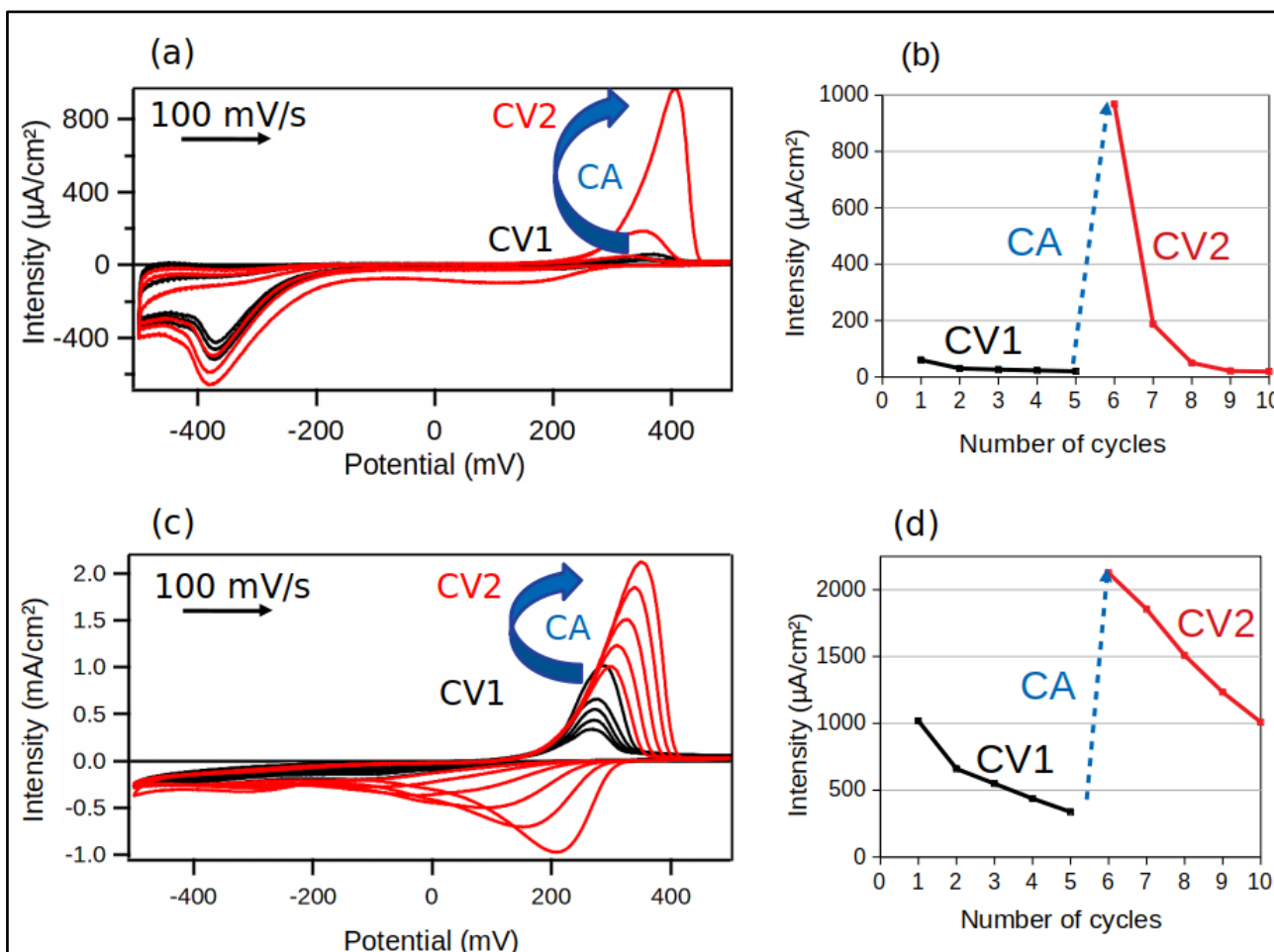


**Figure 6.** Cyclic voltammetry before (black, CV1) and after (red, CV2) chronoamperometry (CA)

(0.2V, 2min under white light irradiation) for  $\text{Fe}_2\text{O}_3\text{-Ag}$  (a) and  $\text{TiO}_2\text{-Ag}$  film (c) (Electrolyte:

Na<sub>2</sub>SO<sub>4</sub> 1M) ; Graph of oxidation peak intensity as a function of the number of cycles for Fe<sub>2</sub>O<sub>3</sub>-Ag (b) and TiO<sub>2</sub>-Ag film (d)

The integration of CA (shown in Figure S4) under white light irradiation between two CVs has a clear effect which is that whereas silver redox peak intensity decreased during CV1, the application of a potential of 0.2 V under irradiation restored the redox peaks of silver NPs during CV2. The effect is even greater for Fe<sub>2</sub>O<sub>3</sub>-Ag samples where silver redox peaks disappeared after 5 cycles (CV1) and an oxidation peak of almost 1 mA/cm<sup>2</sup> was obtained after the CA (Figure 6b). However, this increase is short-lived as it returned to its initial state after only 3 cycles (and 5 cycles for TiO<sub>2</sub>-Ag sample, see Figure 6d). Nevertheless, the CA coupled with white light irradiation restored the silver redox peaks. This observation means that silver species (or Ag<sup>0</sup> species, more generally) were in fact still accessible after CV1.

We can also note that the intensity of the redox peaks in the first cycle in CV1 differs from those observed in Figure 5 for both TiO<sub>2</sub> and Fe<sub>2</sub>O<sub>3</sub> samples. This difference is associated with the background of the samples, as the experiments in Figure 5 had been made on new samples, which is not the case for the experiments for Figure 6. It is still interesting to note that the intensity of redox peaks in CV2 returns to that observed in Figure 5, showing the recycling effect.

It is important to emphasize that this phenomenon is only observed for the combination of an applied potential and irradiation. CA without light does not restore silver redox peaks. If we irradiate without applying potential, only a weak recurrence of silver redox can be observed (not shown in this paper). It was also observed that irradiation at other wavelengths (360, 400 or 455 nm) gave the same response, but with variable intensity.

CA is therefore essential. After several CV cycles, the potential of 0.2V is assigned to an anodic peak (Figure 6b). A weak anodic current is indeed observed during CA, as well as an anodic peak when the light is turned on, indicating that oxidation has occurred (Figure S4). We associated this

peak with an easier oxidation of silver NPs under light, thanks to a decrease in  $\text{Ag}^+/\text{Ag}$  potential redox through an excitation by plasmon resonance. A complementary experiment on  $\text{Fe}_2\text{O}_3$ -Ag film, with increasing times for the CA (from 10 seconds to 15 minutes) showed that the longer the CA time, the higher the observed silver redox peak intensity (Figure S5), indicating that more silver species are impacted. When irradiation stops at the end of the CA, a cathodic peak is observed which we associated with a partial reduction of the  $\text{Ag}^+$  ions.

Based on our results, a hypothesis has been made to explain the partial electrochemical inertia of silver. The absence of silver redox peaks after several CV cycles is made possible because a limited part of the electrode is electrochemically active. This area would correspond to the close vicinity of  $\text{TiO}_2$  or  $\text{Fe}_2\text{O}_3$  films with the conductive FTO substrate. During CV, silver is oxidized and diffuses out of this area, leading to the disappearance of silver redox peaks. Nevertheless, as mentioned before, the fact that the molar ratio of  $\text{Ag}/\text{Ti}$  and  $\text{Ag}/\text{Fe}$  only slightly decreases means that not all the silver diffuses out and a significant part remains within the films.

The electroactive area was estimated based on the amount of available metallic silver and the measured current (ESI 3): 28 nm for  $\text{TiO}_2$ -Ag and 23 nm for  $\text{Fe}_2\text{O}_3$ -Ag films. These thicknesses are similar and correspond approximately to the roughness of the FTO crystals, which could mean that only the silver in direct or very close contact to the FTO substrate respond. This is coherent with the fact that both  $\text{TiO}_2$  and  $\alpha\text{-Fe}_2\text{O}_3$  have very limited conductivity and applied potential distribution is intrinsically not constant over the whole depth of the sample, limiting reactivity in the close vicinity of the FTO interface, as observed experimentally as an electroactive area.

To explain the phenomenon observed in the CV-CA-CV sequence, Scheme 2 shows what happened in CV and CA. During CV (Schema 2a), silver NPs are oxidized to  $\text{Ag}^+$ , the electrons (in blue) are collected by the FTO and produce the electrochemical response. Some of these  $\text{Ag}^+$  ions diffuse out of the electro-active area (the red dash rectangle), though electrochemical reduction of

these ions is limited to the close vicinity of the FTO interface, as  $\text{TiO}_2$  and  $\text{Fe}_2\text{O}_3$  have a limited electrical conductivity. The electroactive area being at the origin of the electrochemical response, the decrease in silver in this area leads to a decrease in its redox peaks, as observed after several CV cycles (Figure 5). After a certain number of cycles, no silver redox peaks are observed whereas silver is still largely detected within the film. We therefore assume that silver is then depleted from the electroactive area and is thus no longer available for electrochemical measurement but is still physically present in the upper part of the electrode.

The action of CA under irradiation is complex (Scheme 2b) and we assume that several phenomena occur at the same time. Irradiation has an impact on both the  $\text{TiO}_2$  and  $\text{Fe}_2\text{O}_3$  films and the silver NPs. At a wavelength below the band gap threshold, the semi-conducting film can be excited (UV for  $\text{TiO}_2$  and 590 nm for  $\text{Fe}_2\text{O}_3$ ) and so further increase the film conductivity, thus enlarging the electroactive area. Combined with this effect, silver NPs within the film are excited by plasmonic resonance resulting in electron transfer to the film by the plasmon induced charge separation (PICS) effect and formation of silver ions. This significant amount of silver ions diffuses within the whole film including into the depleted space, situated at the FTO interface. When the period of CA increases, the number of silver ions formed also increases, leading to an enhancement in silver ion diffusion within the films and an increase of silver redox peaks during CV2 (Figure S5). The applied potential during the CA enables a reduction in the number of silver ions near the FTO substrate. The cathodic current observed at the end of CA corresponds to a reduction in  $\text{Ag}^+$  ions in the electroactive area.



To increase our comprehension of silver diffusion and position within the porous film, we analyzed our TiO<sub>2</sub>-Ag sample using ET. This technique provides insight into the 3D location of silver NPs within the thickness of the film, which could reinforce our previous hypothesis.

In a previous experiment, 500 cycles between - 0.5 V and + 0.5 V were made under three different conditions for the TiO<sub>2</sub>-Ag sample: without irradiation, under 360 nm and under white light<sup>25</sup>. The latter was used to excite Ag NPs through plasmon resonance whereas the 360 nm irradiation was used to excite the TiO<sub>2</sub> matrix, thus creating possible electron transfer between TiO<sub>2</sub> and Ag NPs. For all three cases, CV revealed the disappearance of the silver redox peaks but silver NPs could still be observed by the SEM. For CV with light irradiation, a growth of Ag NPs was clearly observed at the surface and was attributed to an electrochemical Ostwald ripening. Despite a decrease in the Ag/Ti ratio, a significant quantity of silver was still present within the films and we suspected that silver species underwent diffusion under electrochemical cycling.

The first sample analyzed by ET was a reference TiO<sub>2</sub>-Ag one which had not been used in any electrochemical experiment. The two others were TiO<sub>2</sub>-Ag films after 500 cycles under 360 nm and under white light exposure, respectively. These samples were chosen as there was a clear evolution in terms of silver NPs, where a new distribution of the silver species could be observed from the initial position towards the film surface. Figure 7 shows the 3D models (top and side views) of the samples where Figure 7 a) and b) show the reference sample, and c) and d) the sample exposed to a wavelength of  $\lambda=360$  nm and finally, e) and f) for the sample exposed to white light. The silver particles are shown in gray and the TiO<sub>2</sub> support in yellow. The side of TiO<sub>2</sub> film that was towards the FTO was easy to identify, being rough compared to the top surface due to FTO crystallinity.

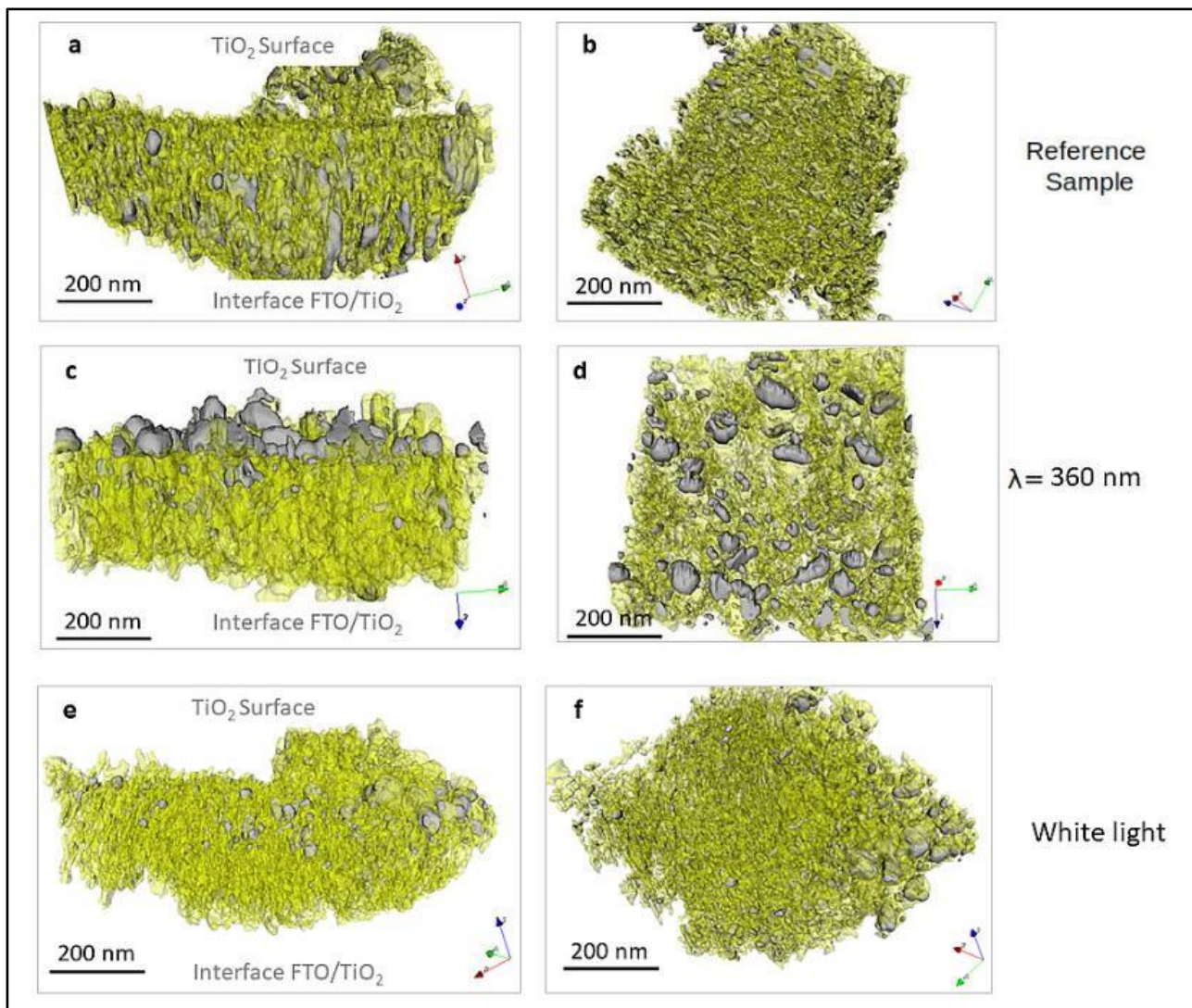


**Figure 7.** 3D Models of TiO<sub>2</sub>-Ag reference sample (a, b), after 500 cycles under  $\lambda=360$  nm (c, d) and after 500 cycles under white light (e, f); Ag NPs are in gray and TiO<sub>2</sub> film in yellow.

In the reference sample (Figure 7 a) and b)), the NPs are homogeneously distributed within the film, having an average size of  $11 \pm 3$  nm. In contrast, samples used under irradiation ( $\lambda=360$  nm or white light) clearly show an accumulation of silver species towards the TiO<sub>2</sub> surface. Quantification of this observation was done and is presented in Figure S6 and Figure 8. The reconstructed volumes were oriented and then seven slices of 30 nm thick were isolated. In each slice, the number of particles and their average size were quantified (Figure 8).

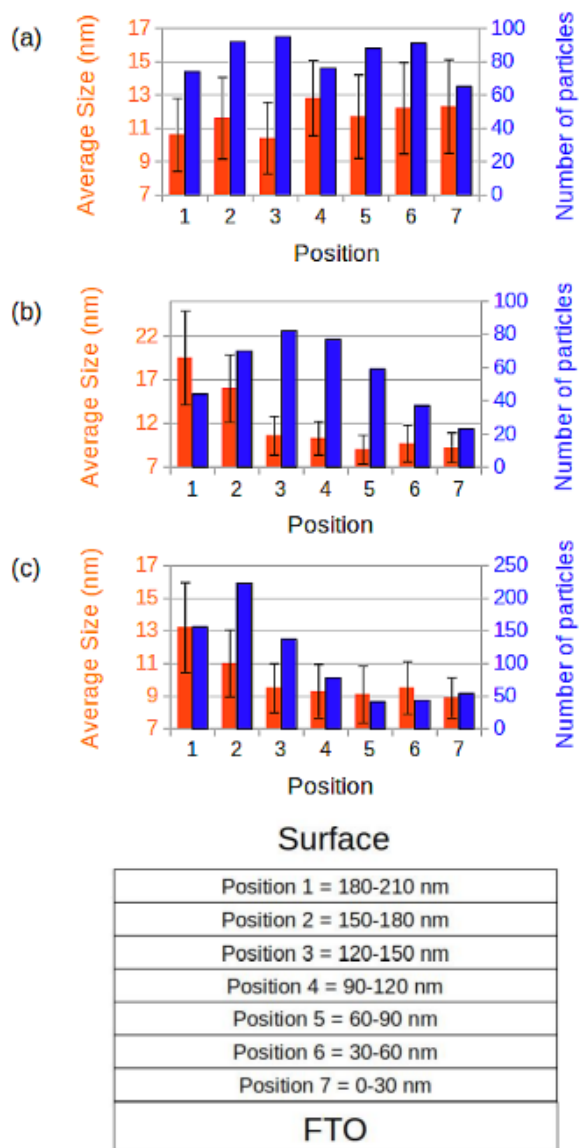


**Figure 8.** Average size and number of Ag NPs depending on their position within the film for (a) reference sample, (b) after 500 cycles under UV irradiation and (c) after 500 cycles under white light irradiation.

It can be clearly seen from Figure 8 that in the vicinity of the FTO substrate (denoted position 7), the number of Ag NPs and their size decrease after electrochemical experiments under irradiation, confirming the visual observation from Figure 7. We might have expected total disappearance of silver NPs in the area in the vicinity of the FTO after electrochemical experiments, but a small quantity of silver is still present. It is therefore important to emphasize here the role of irradiation. In fact, in this experiment, irradiating during CV greatly enhances the diffusion phenomenon with large particles present at the surface of the samples. White light irradiation induces direct excitation

of Ag NPs, leading to electron transfer to the FTO or the matrix and thus the formation of silver ions. Even if the electroactive area is limited to the close vicinity of the FTO, silver ions are generated in the whole sample with irradiation. The enhanced quantity of silver ions increases the Ostwald ripening process with a strong diffusion toward the surface as the bigger particles are situated there. Therefore, two reasons can explain the decrease in the silver specie population in the area close to the FTO: first, the existence of an electroactive area and second, a privileged diffusion toward the surface of silver ions due to the Ostwald ripening process, as shown in Figure 8c.

For the experiment under  $\lambda=360$  nm irradiation, the results are similar. As for the white light irradiation, there is a clear migration and growth of silver species towards the surface and a depletion of the area close to the FTO is observed. This can also be attributed to the electroactive area and Ostwald ripening, the only difference is the formation of silver species. In the case of UV irradiation, Ag NPs and TiO<sub>2</sub> are excited by this irradiation, leading to a direct reduction of silver ions by an electron transfer from TiO<sub>2</sub> to Ag NPs, which can explain why silver NPs are still present in the area close to the FTO even after 500 cycles. Nevertheless, their quantity and size are both smaller compared to the silver present at the top of the sample, emphasizing the diffusion of silver species toward the surface.

From these observations and the previous results of electrochemistry, it is important to differentiate the Ag NPs depending on their localization within the porous film. The Ag NPs of the first type are the ones at the surface, clearly visible by SEM but they correspond to a very small fraction of available particles (3 %). They are electrochemically inactive and bigger than the ones inside the pores. This difference of size drives the diffusion of silver species to the surface due to an electrochemical Ostwald ripening, observed as a growth of the Ag NPs diameter. The Ag NPs of the second type are the ones inside the pores but not in the electroactive area. These ones do not respond either electrochemically, but silver ions formed under irradiation diffuse into the film or to the surface. Also, their numbers increase after electrochemical experiments. The Ag NPs of the third type, which are the ones in the electroactive area, provide most of the electrochemical response. The

oxidation of these Ag NPs into Ag<sup>+</sup> leads to their disappearance from the close vicinity of the FTO. Their size and number therefore decrease after electrochemical experiments, as observed in Figure 8.

These electron tomography experiments have therefore proved the diffusion of silver species toward the surface of the thin film in addition to confirming our previous hypothesis on the existence of an electroactive area. Figures 7 and 8 confirm the decrease in number of silver species present in the area close to the FTO after CV experiments. Furthermore, irradiation, under white light or UV ( $\lambda=360$  nm), induces an increase in Ostwald ripening and diffusion processes leading to the formation of large particles at the surface of the sample.

## CONCLUSION

Two different samples were synthesized using the EISA method: mesoporous TiO<sub>2</sub> and porous Fe<sub>2</sub>O<sub>3</sub>, supporting Ag NPs of 11 to 17 nm in average. The weak intensity of anodic peaks at the beginning of CV experiments combined with the rapid disappearance of the silver redox signal during further cycles, even if silver is still present in the sample, is explained because only a part of the sample is electrochemically responding. In fact, for both samples, we determined that less than 15% of silver is electrochemically active, corresponding to a thickness in the samples of less than 30 nm, located in the close vicinity of the FTO substrate. The position of Ag NPs in porous film is therefore crucial to optimize electrochemical responses. Without irradiation, diffusion is limited to the outside of the electroactive area but does not seem to reach the surface of the sample whereas under UV or white light irradiation, increased diffusion and migration toward the surface is observed, linked to an enhanced Ostwald ripening process. The distribution of silver species outside this electroactive area was clearly highlighted by CV, CA and ET experiments. These techniques represent powerful tools in the understanding and optimized durability of nanomaterial-based

electrodes. These results are likely to be extendable to other materials having low conductivity, such as  $\text{ZrO}_2$ ,  $\text{ZnO}$ , or  $\text{WO}_3$ .

## ASSOCIATED CONTENT

**Supporting Information.** STEM and TEM images of  $\text{TiO}_2$ -Ag and  $\text{Fe}_2\text{O}_3$ -Ag samples; Silver surface estimation; Filled pores rate estimation; IV curves of  $\text{Fe}_2\text{O}_3$  and  $\text{TiO}_2$  without Ag NP; SEM and EDS analysis of  $\text{TiO}_2$ -Ag and  $\text{Fe}_2\text{O}_3$ -Ag after electrochemical experiments; Estimation of silver percentage detected by electrochemistry; CA of  $\text{TiO}_2$ -Ag in a sequence of CV-CA-CV; CV2 of  $\text{Fe}_2\text{O}_3$ -Ag film after different times of CA; Slices of the reconstructed volume of  $\text{TiO}_2$ -Ag samples

## AUTHOR INFORMATION

### Corresponding Author

\* Phone: +33 4 72 43 16 08. E-mail: mathieu.maillard@univ-lyon1.fr

### Author Contributions

The manuscript was written through contributions of all authors. All authors have given approval to the final version of the manuscript.

### Funding Sources

M. Maillard received funding from the LABEX iMUST (ANR-10-LABX-0064) of the Université de Lyon, within the program "Investissements d'Avenir" (ANR-11-IDEX-0007) by the French National Research Agency (ANR) to support this work.

### Notes

The authors declare no competing financial interest.

## ACKNOWLEDGMENT

The authors gratefully acknowledge the Ct $\mu$  platform of electronic microscopy (University Lyon 1) and ClyM ([www.clym.fr](http://www.clym.fr)) for granting the access to the electron microscopes.

## REFERENCES

- (1) Liu, L.; Corma, A. Metal Catalysts for Heterogeneous Catalysis: From Single Atoms to Nanoclusters and Nanoparticles. *Chem. Rev.* **2018**, *118* (10), 4981–5079. <https://doi.org/10.1021/acs.chemrev.7b00776>.
- (2) Linic, S.; Christopher, P.; Ingram, D. B. Plasmonic-Metal Nanostructures for Efficient Conversion of Solar to Chemical Energy. *Nat. Mater.* **2011**, *10* (12), 911–921. <https://doi.org/10.1038/nmat3151>.
- (3) Waiskopf, N.; Ben-Shahar, Y.; Banin, U. Photocatalytic Hybrid Semiconductor-Metal Nanoparticles; from Synergistic Properties to Emerging Applications. *Adv. Mater.* **2018**, *30* (41), 1706697. <https://doi.org/10.1002/adma.201706697>.
- (4) DeSario, P. A.; Pietron, J. J.; Dunkelberger, A.; Brintlinger, T. H.; Baturina, O.; Stroud, R. M.; Owrutsky, J. C.; Rolison, D. R. Plasmonic Aerogels as a Three-Dimensional Nanoscale Platform for Solar Fuel Photocatalysis. *Langmuir* **2017**, *33* (37), 9444–9454. <https://doi.org/10.1021/acs.langmuir.7b01117>.
- (5) Giorgio, S.; Graoui, H.; Chapon, C.; Henry, C. R. Epitaxial Growth of Clusters on Defined Oxide Surfaces-HRTEM Studies. *Cryst. Res. Technol.* **1998**, *33* (7–8), 1061–1074. [https://doi.org/10.1002/\(SICI\)1521-4079\(199810\)33:7/8<1061::AID-CRAT1061>3.0.CO;2-1](https://doi.org/10.1002/(SICI)1521-4079(199810)33:7/8<1061::AID-CRAT1061>3.0.CO;2-1).

- (6) Graoui, H.; Giorgio, S.; Henry, C. R. Shape Variations of Pd Particles under Oxygen Adsorption. *Surf. Sci.* **1998**, *417* (2–3), 350–360. [https://doi.org/10.1016/S0039-6028\(98\)00688-8](https://doi.org/10.1016/S0039-6028(98)00688-8).
- (7) Bratlie, K. M.; Lee, H.; Komvopoulos, K.; Yang, P.; Somorjai, G. A. Platinum Nanoparticle Shape Effects on Benzene Hydrogenation Selectivity. *Nano Lett.* **2007**, *7* (10), 3097–3101. <https://doi.org/10.1021/nl0716000>.
- (8) Innocenzi, P.; Malfatti, L. Mesoporous Thin Films: Properties and Applications. *Chem. Soc. Rev.* **2013**, *42* (9), 4198. <https://doi.org/10.1039/c3cs35377j>.
- (9) Melvin, A. A.; Illath, K.; Das, T.; Raja, T.; Gopinath, C. S. M-Au/TiO<sub>2</sub> (M = Ag, Pd, and Pt) Nanophotocatalyst for Overall Solar Water Splitting: Role of Interfaces. *Nanoscale* **2015**, *7*, 13477–13488.
- (10) Bois, L.; Chassagneux, F.; Battie, Y.; Bessueille, F.; Mollet, L.; Parola, S.; Destouches, N.; Toulhoat, N.; Moncoffre, N. Chemical Growth and Photochromism of Silver Nanoparticles into a Mesoporous Titania Template. *Langmuir* **2010**, *26* (2), 1199–1206. <https://doi.org/10.1021/la902339j>.
- (11) Awazu, K.; Fujimaki, M.; Rockstuhl, C.; Tominaga, J.; Murakami, H.; Ohki, Y.; Yoshida, N.; Watanabe, T. A Plasmonic Photocatalyst Consisting of Silver Nanoparticles Embedded in Titanium Dioxide. *J. Am. Chem. Soc.* **2008**, *130* (5), 1676–1680. <https://doi.org/10.1021/ja076503n>.
- (12) Tobaldi, D. M.; Hortigüela Gallo, M. J.; Otero-Irurueta, G.; Singh, M. K.; Pullar, R. C.; Seabra, M. P.; Labrincha, J. A. Purely Visible-Light-Induced Photochromism in Ag–TiO<sub>2</sub> Nanoheterostructures. *Langmuir* **2017**, *33* (20), 4890–4902. <https://doi.org/10.1021/acs.langmuir.6b04474>.
- (13) Luo, L.; Engelhard, M. H.; Shao, Y.; Wang, C. Revealing the Dynamics of Platinum Nanoparticle Catalysts on Carbon in Oxygen and Water Using Environmental TEM. *ACS Catal.* **2017**, *7* (11), 7658–7664. <https://doi.org/10.1021/acscatal.7b02861>.

- (14) Dubau, L.; Castanheira, L.; Maillard, F.; Chatenet, M.; Lottin, O.; Maranzana, G.; Dillet, J.; Lamibrac, A.; Perrin, J.-C.; Moukheiber, E.; Elkaddouri, A.; De Moor, G.; Bas, C.; Flandin, L.; Caqué, N. A Review of PEM Fuel Cell Durability: Materials Degradation, Local Heterogeneities of Aging and Possible Mitigation Strategies. *Wiley Interdiscip. Rev. Energy Environ.* **2014**, *3* (6), 540–560. <https://doi.org/10.1002/wene.113>.
- (15) Pachón, L. D.; Rothenberg, G. Transition-Metal Nanoparticles: Synthesis, Stability and the Leaching Issue. *Appl. Organomet. Chem.* **2008**, *22* (6), 288–299. <https://doi.org/10.1002/aoc.1382>.
- (16) Khalakhan, I.; Waidhas, F.; Brummel, O.; Vorokhta, M.; Kúš, P.; Yakovlev, Y. V.; Bertram, M.; Dopita, M.; Matolínová, I.; Libuda, J.; Matolín, V. Nanoscale Morphological and Structural Transformations of PtCu Alloy Electrocatalysts during Potentiodynamic Cycling. *J. Phys. Chem. C* **2018**, *122* (38), 21974–21982. <https://doi.org/10.1021/acs.jpcc.8b06840>.
- (17) Brinker, C. J.; Lu, Y.; Sellinger, A.; Fan, H. Evaporation-Induced Self-Assembly: Nanostructures Made Easy. *Adv. Mater.* **1999**, *11* (7), 579–585. [https://doi.org/10.1002/\(SICI\)1521-4095\(199905\)11:7<579::AID-ADMA579>3.0.CO;2-R](https://doi.org/10.1002/(SICI)1521-4095(199905)11:7<579::AID-ADMA579>3.0.CO;2-R).
- (18) Mahoney, L.; Koodali, R. Versatility of Evaporation-Induced Self-Assembly (EISA) Method for Preparation of Mesoporous TiO<sub>2</sub> for Energy and Environmental Applications. *Materials* **2014**, *7* (4), 2697–2746. <https://doi.org/10.3390/ma7042697>.
- (19) Fujishima, A.; Honda, K. Electrochemical Photolysis of Water at a Semiconductor Electrode. *Nature* **1972**, *238*, 37–38.
- (20) Mishra, M.; Chun, D.-M.  $\alpha$ -Fe<sub>2</sub>O<sub>3</sub> as a Photocatalytic Material: A Review. *Appl. Catal. Gen.* **2015**, *498*, 126–141. <https://doi.org/10.1016/j.apcata.2015.03.023>.
- (21) Severance, M.; Dutta, P. K. Evolution of Silver Nanoparticles within an Aqueous Dispersion of Nanosized Zeolite Y: Mechanism and Applications. *J. Phys. Chem. C* **2014**, *118* (49), 28580–28591. <https://doi.org/10.1021/jp5074957>.

- (22) Ivanova, O. S.; Zamborini, F. P. Size-Dependent Electrochemical Oxidation of Silver Nanoparticles. *J. Am. Chem. Soc.* **2010**, *132* (1), 70–72. <https://doi.org/10.1021/ja908780g>.
- (23) Murakoshi, K.; Tanaka, H.; Sawai, Y.; Nakato, Y. Photoinduced Structural Changes of Silver Nanoparticles on Glass Substrate in Solution under an Electric Field. *J. Phys. Chem. B* **2002**, *106* (12), 3041–3045. <https://doi.org/10.1021/jp012443a>.
- (24) Ghosalya, M. K.; Reddy, K. P.; Jain, R.; Roy, K.; Gopinath, C. S. Subtle Interaction between Ag and O<sub>2</sub>: A near Ambient Pressure UV Photoelectron Spectroscopy (NAP-UPS) Investigations. *J. Chem. Sci.* **2018**, *130* (3), 30. <https://doi.org/10.1007/s12039-018-1434-3>.
- (25) Couzon, N.; Maillard, M.; Bois, L.; Chassagneux, F.; Brioude, A. Electrochemical Observation of the Plasmonic Effect in Photochromic Ag Nanoparticle Filled Mesoporous TiO<sub>2</sub> Films. *J. Phys. Chem. C* **2017**, *121* (40), 22147–22155. <https://doi.org/10.1021/acs.jpcc.7b07155>.
- (26) Kremer, J. R.; Mastrorarde, D. N.; McIntosh, J. R. Computer Visualization of Three-Dimensional Image Data Using IMOD. *J. Struct. Biol.* **1996**, *116* (1), 71–76. <https://doi.org/10.1006/jsbi.1996.0013>.
- (27) Gordon, R.; Bender, R.; Herman, G. T. Algebraic Reconstruction Techniques (ART) for Three-Dimensional Electron Microscopy and X-Ray Photography. *J. Theor. Biol.* **1970**, *29* (3), 471–481. [https://doi.org/10.1016/0022-5193\(70\)90109-8](https://doi.org/10.1016/0022-5193(70)90109-8).
- (28) Messaoudil, C.; Boudier, T.; Sorzano, C.; Marco, S. TomoJ: Tomography Software for Three-Dimensional Reconstruction in Transmission Electron Microscopy. *BMC Bioinformatics* **2007**, *8* (1), 288. <https://doi.org/10.1186/1471-2105-8-288>.
- (29) ImageJ <https://imagej.nih.gov/ij/> (accessed Apr 6, 2019).
- (30) Volume Viewer <https://imagej.nih.gov/ij/plugins/volume-viewer.html> (accessed Apr 6, 2019).

- (31) 3D Object Counter <https://imagej.nih.gov/ij/plugins/track/objects.html> (accessed Apr 6, 2019).
- (32) Arganda-Carreras, I.; Fernández-González, R.; Muñoz-Barrutia, A.; Ortiz-De-Solorzano, C. 3D Reconstruction of Histological Sections: Application to Mammary Gland Tissue. *Microsc. Res. Tech.* **2010**, *73* (11), 1019–1029. <https://doi.org/10.1002/jemt.20829>.
- (33) Doube, M.; Klosowski, M. M.; Arganda-Carreras, I.; Cordelières, F. P.; Dougherty, R. P.; Jackson, J. S.; Schmid, B.; Hutchinson, J. R.; Shefelbine, S. J. BoneJ: Free and Extensible Bone Image Analysis in ImageJ. *Bone* **2010**, *47* (6), 1076–1079. <https://doi.org/10.1016/j.bone.2010.08.023>.
- (34) *IUTAM Symposium on Mechanical Properties of Cellular Materials*; Zhao, H., Fleck, N. A., Eds.; Gladwell, G. M. L., Moreau, R., Series Eds.; IUTAM Bookseries; Springer Netherlands: Dordrecht, 2009; Vol. 12. <https://doi.org/10.1007/978-1-4020-9404-0>.
- (35) Okumu, J.; Dahmen, C.; Sprafke, A. N.; Luysberg, M.; von Plessen, G.; Wuttig, M. Photochromic Silver Nanoparticles Fabricated by Sputter Deposition. *J. Appl. Phys.* **2005**, *97* (9), 094305. <https://doi.org/10.1063/1.1888044>.
- (36) Hirakawa, T.; Kamat, P. V. Charge Separation and Catalytic Activity of Ag@TiO<sub>2</sub> Core–Shell Composite Clusters under UV–Irradiation. *J. Am. Chem. Soc.* **2005**, *127* (11), 3928–3934. <https://doi.org/10.1021/ja042925a>.
- (37) de Lara-Castells, M. P.; Cabrillo, C.; Micha, D. A.; Mitrushchenkov, A. O.; Vazhappilly, T. *Ab Initio* Design of Light Absorption through Silver Atomic Cluster Decoration of TiO<sub>2</sub>. *Phys. Chem. Chem. Phys.* **2018**, *20* (28), 19110–19119. <https://doi.org/10.1039/C8CP02853B>.
- (38) Di Liberto, G.; Pifferi, V.; Lo Presti, L.; Ceotto, M.; Falciola, L. Atomistic Explanation for Interlayer Charge Transfer in Metal–Semiconductor Nanocomposites: The Case of Silver and Anatase. *J. Phys. Chem. Lett.* **2017**, *8* (21), 5372–5377. <https://doi.org/10.1021/acs.jpcclett.7b02555>.

(39) Zilberberg, L.; Mitlin, S.; Shankar, H.; Asscher, M. Buffer Layer Assisted Growth of Ag Nanoparticles in Titania Thin Films. *J. Phys. Chem. C* **2015**, *119* (52), 28979–28991. <https://doi.org/10.1021/acs.jpcc.5b09621>.

(40) Couzon, N.; Maillard, M.; Chassagneux, F.; Brioude, A.; Bois, L. Photoelectrochemical Behavior of Silver Nanoparticles inside Mesoporous Titania: Plasmon-Induced Charge Separation Effect. *Langmuir* **2019**, *35* (7), 2517–2526. <https://doi.org/10.1021/acs.langmuir.8b03617>.

(41) de Carvalho, V. A. N.; Luz, R. A. de S.; Lima, B. H.; Crespilho, F. N.; Leite, E. R.; Souza, F. L. Highly Oriented Hematite Nanorods Arrays for Photoelectrochemical Water Splitting. *J. Power Sources* **2012**, *205*, 525–529. <https://doi.org/10.1016/j.jpowsour.2012.01.093>.

